Online Resource 1: Supplementary Information for "The 2022 Chaos Canyon landslide in Colorado: insights revealed by seismic analysis, field investigations, and remote sensing"

Kate E. Allstadt[1]*, Jeffrey A. Coe[1], Elaine A. Collins[1], Francis K. Rengers[1], Anne Mangeney[2], Scott Esser[3], Jana Pursley[4], William L. Yeck[1], John J. Bellini[4], Lance R. Brady[5]

*corresponding author: kallstadt@usgs.gov
1) U.S. Geological Survey Geologic Hazards Science Center, Golden, CO, USA
2) Université Paris Cité, Institut de Physique du Globe de Paris, CNRS, F-75005 Paris, France and Institut Universitaire de France
3) Rocky Mountain National Park, National Park Service, Estes Park, CO, USA
4) National Earthquake Information Center, U.S. Geological Survey, Golden, CO, USA
5) National Uncrewed Systems Office, U.S. Geological Survey, Denver, CO, USA

Any use of trade, firm, or product names is for descriptive purposes only and does not imply endorsement by the U.S. Government.

Additional method details

UAV-derived digital elevation model

We conducted four flights over the slide area with a DJI Mavic Pro Uncrewed Aerial Vehicle (UAV). The first two flights obtained video footage on 15 July 2022 (flight 1: 11:15am-11:29am MDT; flight 2: 11:39am – 11:52am MDT) and the second two flights obtained still photos (flight 3: 12:12pm-12:26pm MDT; flight 4: 12:29pm-12:39pm MDT). Using the 692 georeferenced still photos (available at Rengers et al. (2023)), we used Agisoft Metashape (v. 1.8.3) (Agisoft 2023) to generate a point cloud of the post-event topography (Fig. S1). We lacked ground control points, so after generating the digital elevation model (DEM) using just the UAV global positioning system (GPS) location information, we aligned to the USGS National Map's 3D Elevation Program (3DEP) pre-event 1-m lidar DEM, which was collected in 2020 (U.S. Geological Survey 2022), using the CloudCompare (EDF R&D 2023) software. We did this using 14 manually picked point pairs on landmarks in the unchanged areas distributed closely around the perimeter of the landslide to maximize the alignment in the landslide area and to avoid aligning to warped areas on the edges of the UAV-based point cloud. The automated iterative closest point (ICP) algorithm did not work well in this case, likely because of warping on the edges. To estimate the uncertainty of the aligned post-event elevations, we computed vertical differences using the Multiscale Model to Model Cloud Comparison (M3C2) tool (Lague et al. 2013) in CloudCompare and found that in stable areas, the mean difference was 0.69 m and the standard deviation was 2.5 m. The differences are spatially correlated, so for error propagation purposes for the volume calculations, we quantified the spatial correlation of the elevation differences in the stable areas by constructing an empirical semivariogram by randomly sampling 120,000 pairs of points from the M3C2 vertical difference point cloud, binning the absolute value of the difference of the elevation change between each pair of points into an average for each of 30 log-spaced bins, and then using non-linear least-squares to fit a semivariogram model. This semivariogram process was done in Python, curve fitting was done using SciPy's (Virtanen et al., 2020) curve_fit function. We found that an exponential shape fit best, and

retrieved a range of 165 m (beyond which the difference points are no longer correlated) and a sill of 6.7 m. We merged the aligned post-event point cloud into the pre-event lidar, minimizing seams by clipping along minimums in the difference and created a 1-m DEM that merges the area covered by the UAV point cloud with the pre-event 1-m lidar DEM, as this is needed for the runout modeling presented in the study. The post-event point cloud and DEM is available at Rengers et al. (2023).
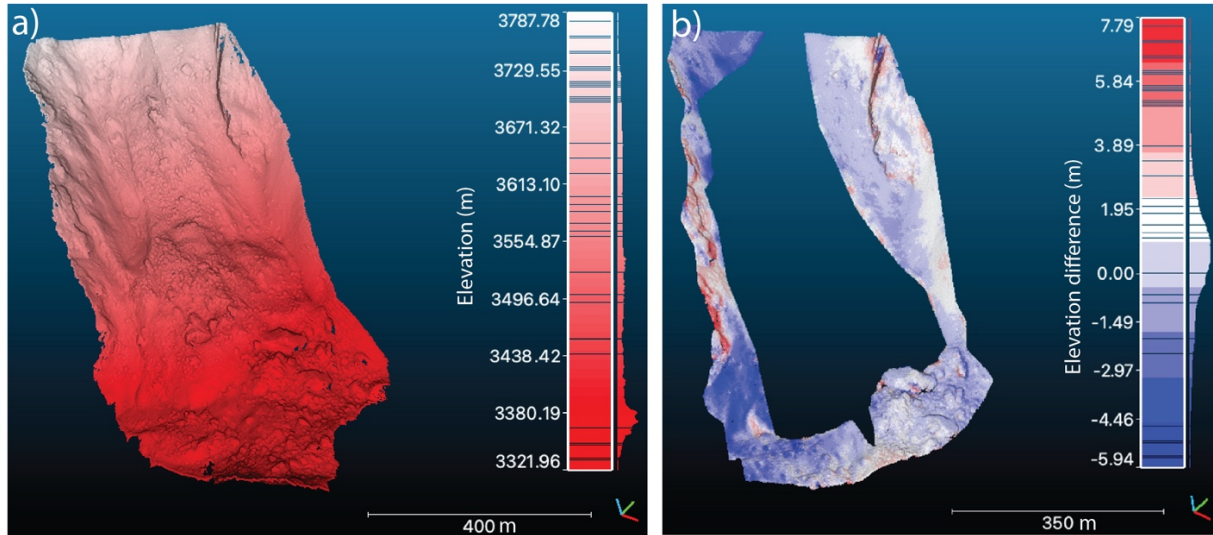

Fig. S1 *(a) Image of the post-event point cloud shaded by elevation in a relative coordinate system and (b) Vertical difference of the stable areas that did not change between the pre-event (2020) airborne lidar DEM and UAV flights. Relative coordinate system used. Histograms on right edge of colorbars show the distribution of elevation and elevation differences.*

Volume estimate

As described in the main text, we had to extrapolate the sliding plane below the deposits to estimate the volume because the material did not completely evacuate the source area. We did this by fitting logarithmic spiral profiles between the part of the source area void of deposits from the post-event DEM, and the surface of the pre-event slope below the source area along cross-sectional profiles spaced every 20 m (Fig. S2a). This was done by taking the slope angle of the 40-m long part of the cross section closest to the gap on either side and solving for the logarithmic spiral segment that best fit the entry and exit angles and locations on either side of the gap in the profile using non-linear least squares. A logarithmic spiral is a suitable shape to assume when other information about the geometry is not available because it is hypothesized to be the curve along which a failure will happen in homogeneous material (Terzaghi et al. 1996). In the case of the Chaos Canyon landslide, this slip surface was likely the surface between overlying debris and underlying bedrock. For most of the landslide, this surface is fairly planar, as might be expected in the fractured Proterozoic rocks that are present at the site. The surface curves at the headscarp and toe, where rock is exposed, and the material travels over the valley floor. The resulting profiles (e.g., Fig. S2b) look smooth and are consistent with typical landslide cross sections that might be drawn by hand by an expert (e.g., Jaboyedoff et al. 2020).
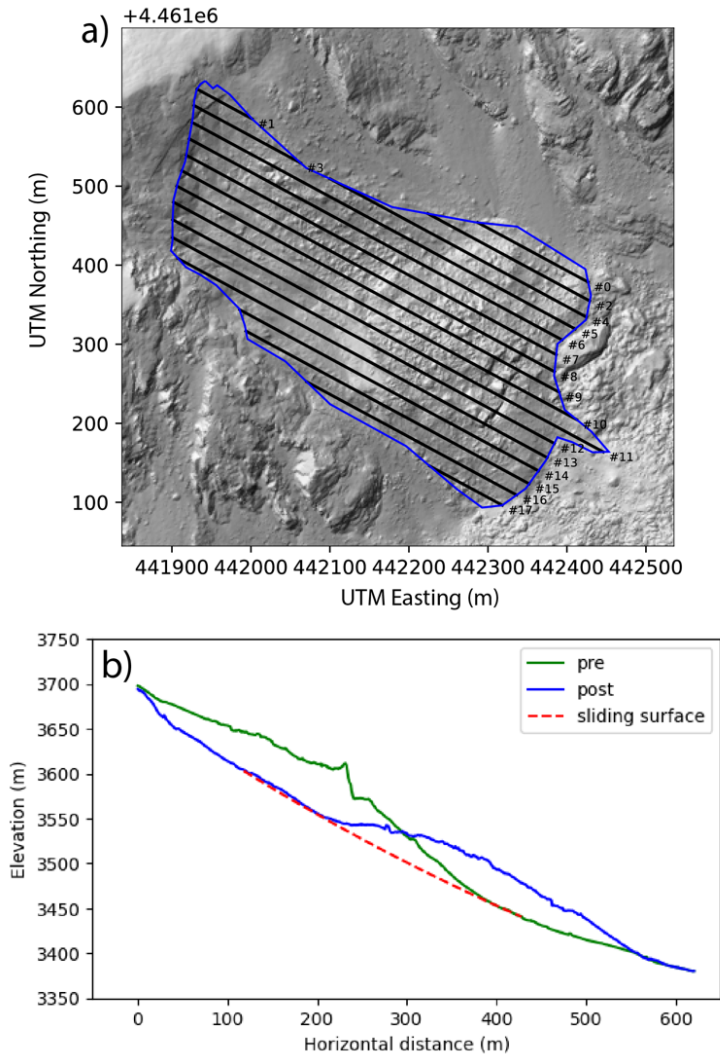
Fig. S2 *(a) Location of profile lines (black) used to interpolate the failure surface, the landslide is outlined in blue. (b) the pre- and post-event profiles (green and blue) along profile line 11 and the resulting interpolated sliding surface (red).*

We then interpolated a piecewise linear three-dimensional (3D) function between these profiles and the surrounding topography, using the exposed part of the source area from the post-event DEM and the exposed part of the runout area from the pre-event DEM and smoothing the area in between that was interpolated from the log spiral profiles with Gaussian smoothing (with a standard deviation of 10 m) to smooth out sharp edges from the interpolation, yielding a DEM of the sliding surface. Differencing the pre- and post-event DEMs from this sliding surface yields the vertical thickness distribution of the source area and deposits (Fig. 7c, e main text). We multiplied the thickness distributions by the area of each cell (1 m^2) and summed over the slide area to estimate the total volume for both the source area and the deposits. We propagated the uncertainty using standard methods by assuming a constant standard deviation of 2.5 m and using the semivariogram model described above (range 165 m, sill 6.7 m) to construct the covariance matrix required to estimate the standard deviation of the volume, given that the errors are spatially correlated.

3

Displacement monitoring of Two Towers

We estimate a time series of displacement over about two decades using the "Two Towers" rocks (Fig. 1, main text), using orthorectified aerial imagery from USGS EarthExplorer (Digital Orthophoto Quadrangles (DOQ), National Agriculture Imagery Program (NAIP)), and satellite imagery from Planet Labs (PlanetScope), and Maxar (Worldview) that was orthorectified by the vendors. We selected 13 images collected between 1990 and 2022 (Table S1) that were well-orthorectifed based on a comparison with stable features outside of the landslide slope. We used the Two Towers features instead of other persistent features on the slope because they are large, distinct, and easy to delineate even in lower-resolution imagery. For each image, we digitized a polygon around the Two Towers and used QGIS (QGIS.org, 2022) to compute the centroid of each polygon. We then measured displacement distance between each pair of time-adjacent points, assuming the first image from August 1990 as the zero reference point, and then using a linear line segment connecting the two centroids. Average velocity is determined by dividing that distance by the time between those two images. Distance uncertainties are measured from the centroid of our best estimate of the polygon to the farthest centroid of alternate plausible polygons, based on image resolution. The full results are shown in Fig. 4 of the main text and some images and centroids are shown in Fig. 3. Fig. S3 below shows images and polygon outlines for some additional dates.

Table S1 *List of images used for Two Towers displacement analysis*

| Date of Image (MM-DD-YYYY)	Image ID	Source	Resolution
08-27-1990	DI00000000838999	USGS EarthExplorer (DOQ)	1 m
10-12-1999	DI00000100224602	USGS EarthExplorer (DOQ)	1 m
08-08-2009	M_4010543_SE_13_1_20090808	USGS EarthExplorer (NAIP)	1 m
05-26-2012	10300100186B6700	Maxar (Worldview-2)	0.5 m
09-05-2016	20700106D5541100	Maxar (Worldview-3)	0.36 m
07-28-2017	20170728_170556_0f10	Planet Labs (PlanetScope)	3 m
07-29-2018	20180729_171959_1025	Planet Labs (PlanetScope)	3 m
08-14-2019	20190814_172235_0e0f	Planet Labs (PlanetScope)	3 m
07-29-2020	20200729_173419_1040	Planet Labs (PlanetScope)	3 m
07-11-2021	20210711_171229_02_2276	Planet Labs (PlanetScope)	3 m
10-25-2021	20211025_172915_1038	Planet Labs (PlanetScope)	3.125 m
06-13-2022	20220613_172735_30_248e	Planet Labs (PlanetScope)	3 m
06-21-2022	20220621_172626_55_2475	Planet Labs (PlanetScope)	3 m
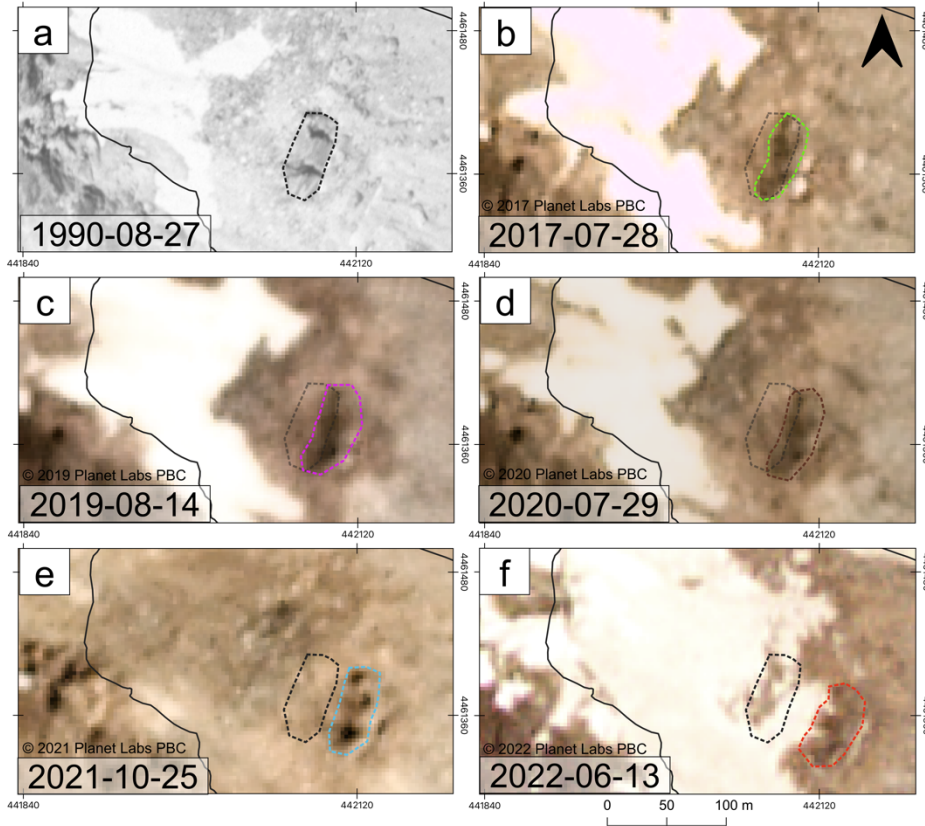
Fig. S3 *Satellite imagery illustrating the movement of the "Two Towers" rocks since 1990. Dashed polygons approximately outline the "Two Towers" region. Solid black polygon represents the outline of the 28 June 2022 event. Each panel contains the polygon from the 1990 image and current image's polygon. (a) Imagery from USGS EarthExplorer. (b-f) Imagery from Planet Labs.*

Seismic investigation

As described in the main text, we initially located the earthquake-like signal that occurred at 4:32:05 pm MDT (22:32:05 UTC) to be within a few kilometers of the landslide. Due to its occurrence about a minute before the main landslide, we hypothesized that it was related to the landslide initiation process and investigated further. Initially, we conducted a search for repeating earthquakes (earthquakes with similar waveforms because they share similar locations and mechanisms). Although rare, there are a few instances where small earthquakes occur that are associated with ice fracturing or stick-slip motion as sliding accelerates prior to a landslide (e.g., Caplan-Auerbach and Huggel 2007; Yamada et al. 2016; Poli 2017; Toney et al. 2021). Such signals related to stick-slip sliding behavior often repeat. Repeated small amplitude vibrations may also affect slope stability in some situations (e.g., Durand et al. 2018; Léopoldès et al. 2020). Therefore, we used a subspace detector (Harris, 2006) that is integrated with National Earthquake Information Center data streams (e.g., Benz et al. 2015) to look for previous events with similar waveforms. We used 25 seconds of data from all three components of the signal of the 28 June 2022 earthquake-like event from station ISCO (Fig. 2, main text) as the template waveform and searched the time period from four months prior to the landslide, to about one month after. We found 38 instances of signals with similar waveforms (cross-correlation coefficient (CC) >0.2), 20 with CC>0.5 (Fig. S4, Table S2). Puzzlingly, most of these repeats occurred around 4:30 pm local time on weekdays,

and several occurred after the landslide when we would not expect to see more repeats of a signal related to landsliding. This repeating schedule indicated that the signal was probably related to human activity, most likely blasting. Even though the source was not from the landslide, the spatiotemporal coincidence indicated this human activity may have affected the landslide behavior, so we continued to investigate the source.
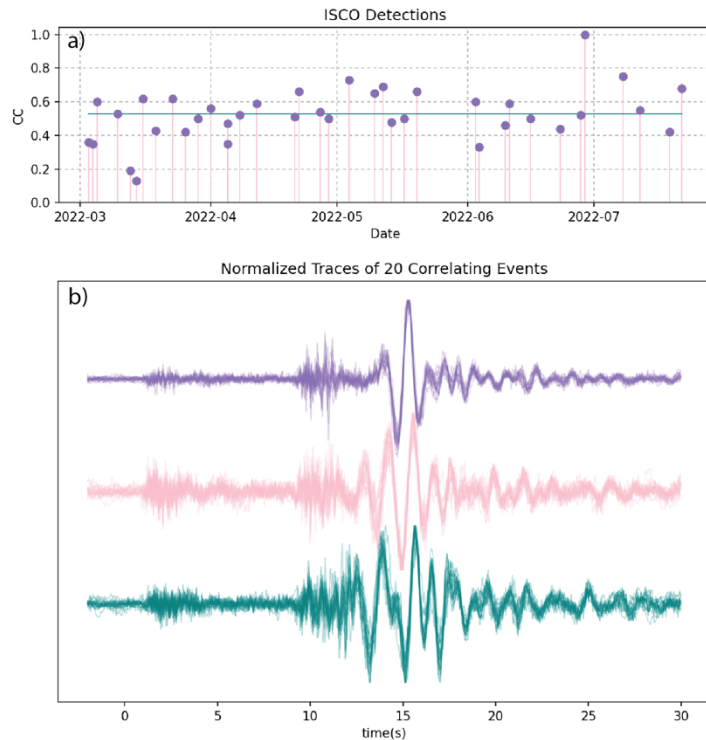

Fig. S4 *Results of the repeating earthquake search from 1 March to 21 July 2022, using the 28 June 2022 earthquake-like signal recorded on all three components of the ISCO station (Fig. 2, main text) as a template. (a) Shows the correlation coefficient (CC) between each detection and the template. The dot with a CC of 1 is the template event. (b) Shows the superimposed waveforms of the 20 most well-correlated events (CC >0.5) on three components, BHZ (purple, top), BH1 (pink, middle) and BH2 (green, middle).*

The most puzzling thing about this earthquake-like source was that its location fell in the middle of a vast wilderness area where there are no quarries and blasting is not allowed. Rocky Mountain National Park (RMNP) confirmed that there was no blasting occurring during that time window in the park (e.g., for road or trail construction). A large transmountain water tunnel, the Adams tunnel, passes almost directly below the landslide at several hundred meters depth so we checked with the Bureau of Reclamation whether there was construction or other activity in that tunnel at these event times that could be a potential source, but there was not. Still emptyhanded, we then tried to improve the location. Because the magnitudes were so small (M_L 1.3-1.6, Table S2), the P- and S-wave arrival times were a little uncertain and only visible on a handful of seismic stations for any of the individual events. This small number of stations resulted in underestimated formal location uncertainties, so to get a better sense for the real location scatter, we located several other occurrences of the repeat, and we also aligned and stacked the repeating earthquake signals to pick more accurate phase arrival times and

recalculated the location. These analyses indicated that the location was poorly constrained in the east-west direction (likely because the stations that detected the blast were mostly to the north and south of the source), and that the location was likely somewhere within an area spanning from the landslide, to ~40 km to the east. We called several quarries in that area and contacted state blasting regulators and finally confirmed that the time of the seismic events we detected were consistent with blast times at the construction site of the Chimney Hollow Reservoir (Fig. 2, main text).

Table S2 *List of events detected with cross-correlation coefficient >0.5*

Date	Time (UTC)	Local magnitude	Correlation coefficient
3/4/22	23:29:42	1.55	0.60
3/9/22	21:57:46	1.42	0.53
3/15/22	22:31:20	1.4	0.62
3/22/22	22:29:36	1.52	0.62
3/31/22	22:30:04	1.6	0.56
4/7/22	22:29:52	1.39	0.52
4/11/22	22:49:33	1.61	0.59
4/20/22	22:29:58	1.41	0.51
4/21/22	22:30:51	1.64	0.66
4/26/22	22:30:15	1.54	0.54
5/3/22	22:29:28	1.48	0.73
5/9/22	22:30:27	1.47	0.65
5/11/22	22:49:21	1.48	0.69
5/19/22	22:30:04	1.51	0.66
6/2/22	22:31:12	1.54	0.60
6/10/22	22:31:41	1.51	0.59
6/27/22	22:30:20	1.48	0.52
6/28/22	22:32:04	1.5	1.00*
7/7/22	22:34:45	1.54	0.75
7/11/22	22:30:40	1.46	0.55
7/21/22	20:41:03	1.46	0.68

*indicates the template event

Video-based landslide velocity estimate

We estimated the average landslide velocity from a video taken by a park visitor, Ryan Albert, from near Lake Haiyaha (Fig. 1, main text) that was posted online by several news agencies (e.g., 9news.com 2022). The video was taken in profile view and started when the slide was already underway and concluded as it became enveloped in dust. The "Two Towers" features mentioned in the main text, which are two prominent rocks that were embedded in the landslide slope, were easily visible in the footage so we used these as a reference point for distances. We estimated the width of the Two Towers as viewed from Lake Haiyaha by drawing a line of sight from Lake Haiyaha to the Two Towers polygon based on Planet Labs imagery acquired on 21 June 2022. We then drew several possible widths of the polygon, which are near perpendicular to the Lake Haiyaha line of sight, estimating an average width of 44 m. Between 5 and 13 seconds into the video, the Towers move approximately one width of themselves (44 m) downslope. Divided by a time difference of 8 seconds, results in an along-slope velocity estimate of 5.4 +/- 1.0 m/s. Velocity uncertainty is based on the low and high width estimates (35-51 m) of the Two Towers from the Lake Haiyaha line of sight.

Numerical landslide modeling

We modeled the 28 June 2022 landslide and possible future runout scenarios using SHALTOP, a shallow-water depth-averaged numerical continuum model for granular flows over 3D topography (Bouchut et al. 2003; Bouchut and Westdickenberg 2004; Mangeney et al. 2007; Lucas et al. 2014; Peruzzetto et al. 2021). Due to uncertainties regarding internal landslide materials, we used the simplest rheological law available in SHALTOP, the Coulomb friction law, which assumes a single constant effective friction coefficient μ=tanδ, where δ is the friction angle. We focus on this law because it has only one parameter that can vary, and it is useful to compare that best fitting effective friction angle to estimates from the deposits.

To model the 28 June landslide, we downsampled all input layers to 5-m resolution to reduce both computational load and model instabilities that can arise from excess roughness, then subtracted the source thickness from the DEM and smoothed the resulting sliding surface using a gaussian blur to further reduce model instabilities. SHALTOP works in a slope normal coordinate system, so we multiplied the vertical source thickness by the cosine of the slope angle at each grid cell to estimate slope normal thicknesses. We then ran simulations by looping over a range of friction angles and particle sizes (when applicable) to find the parameters and rheological model that minimized the root mean squared error ($RMSE$) of the modeled deposit thickness distribution relative to the measured one, and that also maximized the trimline ratio (tr) (Galas et al. 2007), which is the ratio of the overlapping modeled and measured deposit footprints to the union of both footprints. To consider both fit metrics equally in choosing the best performing models, we minimized a combined fit metric normalized to the range of fit values from all simulations using:

$$\frac{RMSE - \min(RMSE_{allruns})}{\max(RMSE_{allruns}) - \min(RMSE_{allruns})} + \frac{\max(tr_{allruns}) - tr}{\max(tr_{allruns}) - \min(tr_{allruns})}$$

in which the value closest to zero indicates the best fit.

We focused on conservative model scenarios of potential future mobilizations of the deposits of the 28 June landslide by modeling the mobilization of the entirety of the deposits. Therefore, we used the same sliding surface as we did for the 28 June event and used the final deposit thickness distribution to define the starting volume. Predicting the runout distance of a slide mass a priori is an ongoing challenge in landslide science (e.g., Hungr et al. 2005; Delannay et al. 2017; McDougall 2017; Peruzzetto et al. 2020). In this study, we used statistical relationships fit to historical datasets of volume and mobility, quantified by vertical drop height/horizontal runout length (H/L) (also known as Heim's ratio, (Heim 1932; Hungr et al. 2005)) to estimate a range of effective friction coefficients (μ). Mobility has long been indexed using the H/L ratio, which is measured from the very top of the headscarp to the end of the toe and is equal to the tangent of the reach angle (also known as the travel angle, or the fahrböschung) (Hungr et al. 2005). The H/L ratio has an observed inverse correlation with volume (i.e., larger landslides are more mobile) and has commonly been interpreted as an estimate of μ (Heim 1932; Scheidegger 1973; Corominas 1996; Lucas et al. 2014). However, it is an imperfect estimate of μ as shown by the different analytical formula for the two quantities (Lucas et al. 2014) and because H/L data are scattered due to factors such as ill-defined conventions and the influence of obstructions and deflections along the path (e.g., Corominas 1996; Legros 2002). H/L is also just approximating the actual desired measurement, which is the H/L of the center of mass (H/L$_{cm}$), but is used more because H/L is far easier to measure than H/L$_{cm}$.

H/L$_{cm}$ can be shown analytically to be equal to μ for a rigid block slide (Hsü 1975; Hungr et al. 2005; Lucas et al. 2014).

Lucas et al. (2014) found that μ was approximately equal to H/L for a set of historical landslides when their volumes were large (>10^6 m^3), and this was validated using the same numerical landslide model used in this study (SHALTOP). Therefore, for modeling of the remobilization of the deposits in Chaos Canyon, assumed that the H/L value was a reasonable estimate of μ and handled its uncertainty by estimating a range of H/L values (and thus a range of μ) from historical datasets that are most representative of our volume and scenario. Statistical comparisons of H/L datasets show that different types of landslides tend to have different mobility-volume relationships that reflect differences in the underlying physics and materials. For example, wet debris flows tend to have higher mobility (lower H/L and μ) than translational landslides or rock falls (Corominas 1996; Legros 2002), and landslides in volcanic settings tend to have higher mobility than non-volcanic settings (Hayashi and Self 1992). There are not enough debris slides or slides over rock glaciers in the historical databases to derive a relationship specific to the Chaos Canyon landslide. Instead, we selected a set of H/L measurements for 32 non-volcanic subaerial landslides originally compiled by Hayashi and Self (1992), also later used by Legros (2002), to determine a mean and 95% range of μ for our runout simulations. We re-regressed the original data and confirmed nearly the same equation as Hayashi and Self (1992):

$$\log(H/L) = -0.7874 - 0.1548(\log V),$$

where V is volume in cubic kilometers. Because the data have substantial scatter, to capture that uncertainty we estimated the 95% certainty range of the fit to the H/L and volume data by randomly resampling 16 of the datapoints 1000 times and refitting the regression line, and then taking the central 95% range of those line fits at each volume interval within the range of the data (Fig. S6 inset).

Runout modeling results

28 June 2022 landslide

We first modeled the main landslide event using SHALTOP as described above to provide a reality check on the scenario simulations. Even though evidence implies sliding along a failure plane was the primary mode of failure and thus a granular flow model may not be fully appropriate, we found the best fit between the observed and modeled deposit when we assume δ=29.5° (Fig. S5, see Online Resource 3 for animation). Notably, 29.5° is quite close to the effective friction angle estimated from the H/L$_{cm}$ (δ=30°) and not much higher than that estimated from H/L (δ=28°). However, in all simulations, the velocities were too high, the onset too sudden, and the duration of the landslide too short when compared to seismic and video-based evidence (Fig. S5e). For example, the seismic signal builds up gradually before peaking and this implies a more gradual initiation than the model simulates. Excessive initial velocities are a known issue with this and other models that use the shallow-water approximation and assume hydrostatic pressure (e.g., Lucas et al. 2014; Garres-Díaz et al. 2021). However, this mismatch may also be partially due to the misfit between a granular flow model and an initial coherent sliding mechanism. For example, the best fitting friction angle of 29.5° is substantially higher than the angles found for this landslide volume empirically for simulations of landslides having a granular type behavior (Favreau et al. 2010; Lucas et al. 2014).
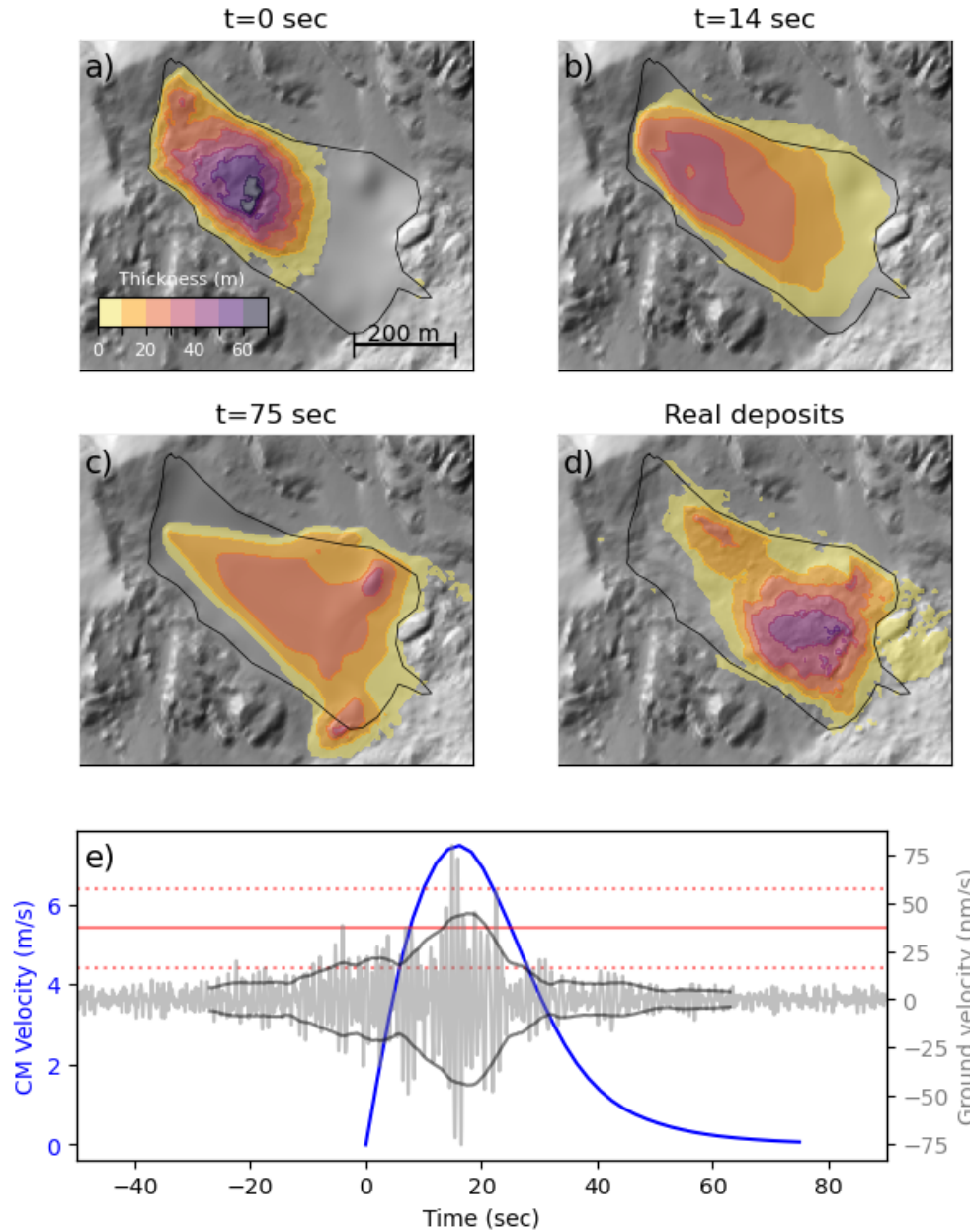
Fig. S5 *Best-fitting SHALTOP model of the main 28 June 2022 landslide (δ=29.5°) at three different time windows (a-c), compared to the real distribution of the deposits (d). (e) compares the velocity of the center of mass (CM) of the model (blue), showing the modeled event duration compared to the vertical component seismic signal recorded at ISCO (0.7-3 Hz filter) (gray) and its smoothed envelope (dark gray). Time is relative to the start time of the model simulation at t=0. The seismic signal is shifted so the peak aligns with peak model velocity. Red lines indicate the slide velocity and uncertainty range estimated from the eyewitness video.*

The results of all simulations are summarized in Table S3. We note that several simulations, including the best fitting one, give an H/L ratio equal to the measured value (0.54), but the distribution of the deposits is too spread out in all of the simulations. These observations are very similar to findings by

Brunet et al. (2017) and Poulain et al. (2023) for other landslides. We compare the final distribution of the deposits for the best fitting model to the real deposits in Fig. S5c, d. An animation of the best fitting simulation is included in Online Resource 3. Shallow depth-averaged models are known to overestimate the velocity due to the hydrostatic pressure assumption (Garres-Díaz et al. 2021) and to have shorter duration because the mass stops more suddenly due to depth-averaging, ignoring the complexity of the stopping phase (Mangeney-Castelnau et al. 2005).

Table S3 Summary of parameters for model simulations, ordered by the lowest (best) to highest fit metric.

Friction angle (δ)	Root mean squared error (m)	Trimline ratio	H/L	Fit metric
29.5°	2.804	0.625	0.54	0.173
29°	2.693	0.604	0.53	0.182
30°	2.993	0.644	0.54	0.187
28°	2.763	0.552	0.51	0.283
32°	4.135	0.630	0.54	0.480
26°	3.689	0.410	0.49	0.738
24°	5.051	0.267	0.46	1.295
22°	6.046	0.175	0.45	1.682
20°	6.504	0.096	0.44	1.921
18°	6.465	0.048	0.43	1.991

Runout modeling of worst-case scenarios

To examine the hazard that a worst-case scenario remobilization could pose to areas farther down the canyon that are frequented by climbers and hikers, we conducted runout modeling using the methods described above. To make a conservative assessment, we modeled the remobilization of the entire volume of the debris slide deposits (2.1×10^6 m^3), although this is an unlikely scenario as discussed in the main text. However, we also make the less conservative decision of assuming no entrainment or liquefaction along the travel path due to the extreme coarseness of the path material.

Using the best estimate and 95% uncertainty range derived from the Hayashi and Self (1992) H/L database described in the methods above (Fig. S6 inset, green lines) gave us a best estimate H/L value of 0.42 (δ=22.8°), and a 95% range of 0.35-0.52 (δ=19.2-27.5°) for a volume of 2.1 million m^3. We then use the mean and 95% range of the above H/L values directly as the effective friction coefficient, which is equal to the tangent of the effective friction angle (δ), in three different SHALTOP simulations that illustrate a range of possible runout scenarios (Fig. S6). The mean scenario (δ=22.8°) travels at most 275 m past the end of the existing deposits, and much of the material remains in two depressions south and east of the toe. These topographic sinks have the practical effect of reducing the mobility such that the H/L of the mean simulation is higher (0.47) than the H/L value that was used to estimate the friction coefficient from historical data (0.42) (black dashed line, Fig. S6b). The low mobility (δ=27.5°) scenario barely leaves the source area, which makes sense given that the δ is only slightly lower than the best fitting value of δ=29.5° for the 28 June landslide simulation. The high mobility simulation (δ=19.2) travels farther and does just barely reach an area informally known as "the Meadow," where climbers

sometimes congregate (Fig. S6c). But this simulation also has a much higher H/L value (0.45) and thus shorter runout distance than the H/L value that we used as the friction coefficient (0.35) (black dashed line, Fig. S6c) because much of the material is deposited in the same topographic sinks. Animations are included in Online Resources 4-6.
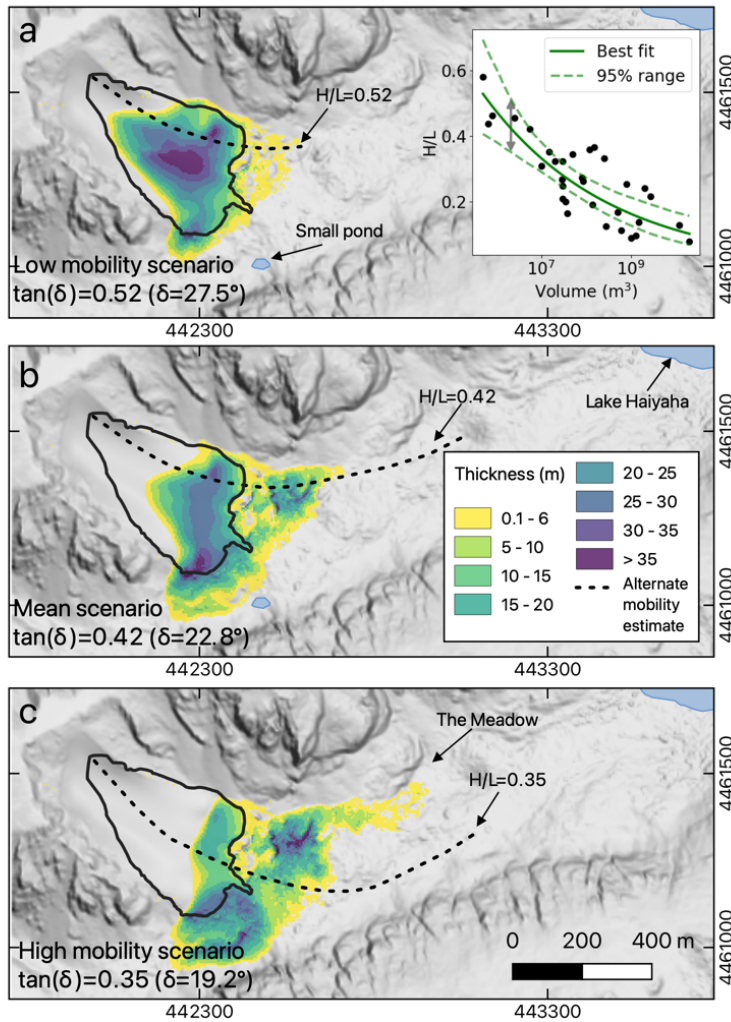

Fig. S6 *Final thickness of deposits of SHALTOP simulations of the remobilization of the entire deposit using preferred mobility estimation approach. The inset figure illustrates the regression model fit of the relationship between H/L and landslide volume for non-volcanic subaerial landslides compiled by Hayashi and Self (1992) in solid green, the dashed lines indicate the 95% certainty range for the regression fit that we estimated using bootstrapping. The gray arrow spans the 95% range of H/L values at the volume of the deposits (2.1 million m³), which is the range assumed as the effective friction coefficient for the simulations. The higher end of the range (low mobility) is shown in panel a, the lower end of the range (high mobility) is shown in panel c, and panel b shows the simulation corresponding to the mean scenario. As an alternate mobility estimate, we show with black dashed lines where the simulation would*

reach if we had lowered the friction angles until the H/L of the simulation reached the H/L values for this 95% range. Coordinate reference system NAD83(2011)/UTM zone 13N.

Although our best estimates for the range of likely runout distances of a remobilization of the entirety of the slide deposits presented above indicate moderate mobility that is modulated by the undulating topography of the rock glacier, there are alternate approaches to selecting a friction angle for the runout modeling that produce longer runouts. We present three of these alternate scenarios in this section. Corresponding animations are included as Online Resources 7-9.

For the first simulation, we use the same equation and set of historical data as the main text, non-volcanic subaerial landslides (Hayashi and Self 1992), which gives an H/L for our landslide volume of 0.42. However, instead of using that H/L value as the effective friction coefficient (μ), we run simulations at a range of friction angles until the runout matches that H/L value. We use the μ(I) rheology instead of Coulomb for this scenario because that rheology performed better for the main landslide event and we are not tied to a single specific friction angle. This approach results in deposits reaching a larger thickness in the Meadow (Fig. S7b) than the high mobility scenario from the main results (Fig. S6c), but not traveling much past it, as well as a second leg of the deposits that flows down the south side of the valley. This approach is not ideal and likely provides an overestimate because forcing the H/L value match negates the influence of the unusual runout path topography on mobility.

For the second alternate simulation, we consider an empirical relation by Lucas et al. (2014) that directly estimates μ, by $\mu = V^{-0.0774}$, where landslide volume, V, in cubic meters, was calibrated on a broad set of 171 landslides from Earth and other planets and was validated for a subset of about 40 landslides using SHALTOP. We run this model because unlike our other approaches, it provides a direct estimate of μ and thus does not require the assumption that $H/L \approx \mu$. It also was validated with the same model used in this study. We included this simulation to represent what the average landslide runout might be in the absence of information or assumptions about landslide style or setting, using μ=0.32 (δ=18°). The resulting simulation (Fig. S7b) is similar to the high mobility scenario presented in the main results (Fig. S6c). This method likely overestimates mobility, however, because many more mobile types of landslides and settings are included in the dataset.

Alternatively, as an upper bound, we consider the scenario where the deposits are sufficiently saturated that they mobilize into a debris flow. As stated in the main text, we do not think that the deposits and runout path characteristics are conducive to this style of movement so this is likely a vast overestimate of mobility, but there are enough unknowns that it is within the realm of possibility. We utilize the relation by Corominas (1996) based on 71 historical debris flows, $\log\left(\frac{H}{L}\right) = -0.012 - 0.105 \log(V)$, where volume is in cubic meters, to estimate H/L and then we assume that value (μ=0.21, δ=12°) as the coefficient of friction. This simulation is, as expected, the most mobile of all the scenarios (Fig. S7c). Deposit thicknesses reach ~30 m in the Meadow, and a second branch of the flow traveling down the south side of the valley reaches within ~250 m of Lake Haiyaha.

All alternatives show runout paths that do inundate the Meadow, and the debris flow simulation reaches within about 250 m from Lake Haiyaha. However, based on our experience, these alternative

higher mobility simulations, and especially the debris flow simulation, are overestimating mobility and are not very realistic due to the large grain sizes and complex runout path characteristics.
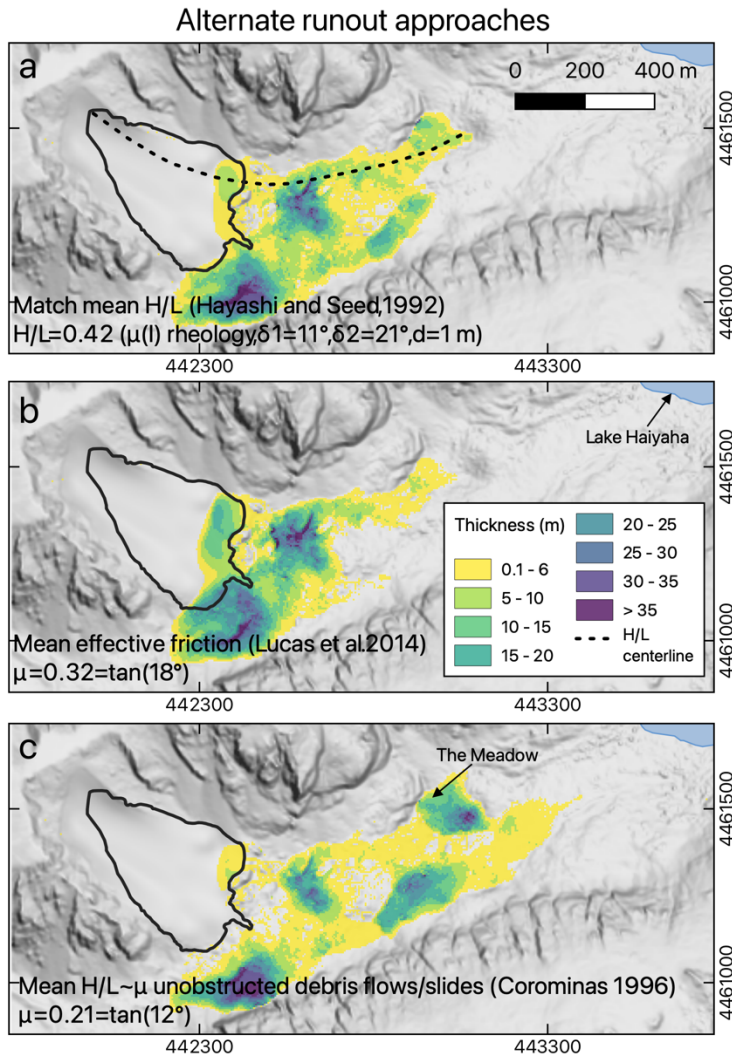

Fig. S7 *Alternate SHALTOP runout modeling simulations of the remobilization of the entirety of the deposits. (a) Matching runout distance by adjusting friction angles until it reaches an H/L value that exactly matches the H/L value from Hayashi and Self (1992) non-volcanic subaerial landslide equation. Dashed black line indicates the profile line along which H/L was calculated. (b) Using the effective friction angle from equation in Lucas et al. (2014) for all landslides in the database (earth and planetary). (c) Estimating the effective friction angle using the H/L estimate for debris flows from Corominas (1996). Coordinate reference system NAD83(2011)/UTM zone 13N.*

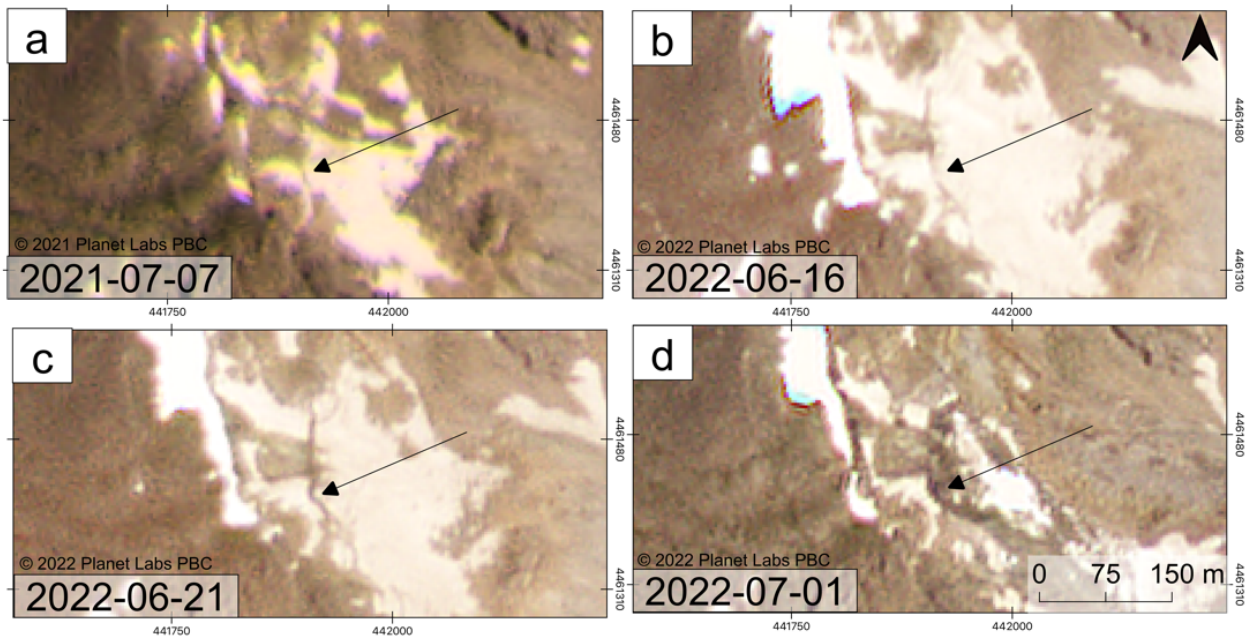## Additional photos and figures

Fig. S8 *PlanetScope satellite imagery of fracture near the top of the snowfield on Hallett Peak. Small fractures first noticeably appeared in this region in the summer of 2021 but were not as pronounced or continuous as in 2022. (a, b) Fracture is barely visible on 7 July 2021, and appears to widen by 16 June 2022. The earliest image where the fracture is visible (regarding snow cover) in 2022 is from 12 June. (b, c) Fracture widens even more between 16 and 21 June 2022. Fracture pattern also appears to change slightly in southern region. (d) The 28 June 2022 event has failed along the fracture as depicted in this post-event image. Coordinate reference system NAD83(2011)/UTM zone 13N.*
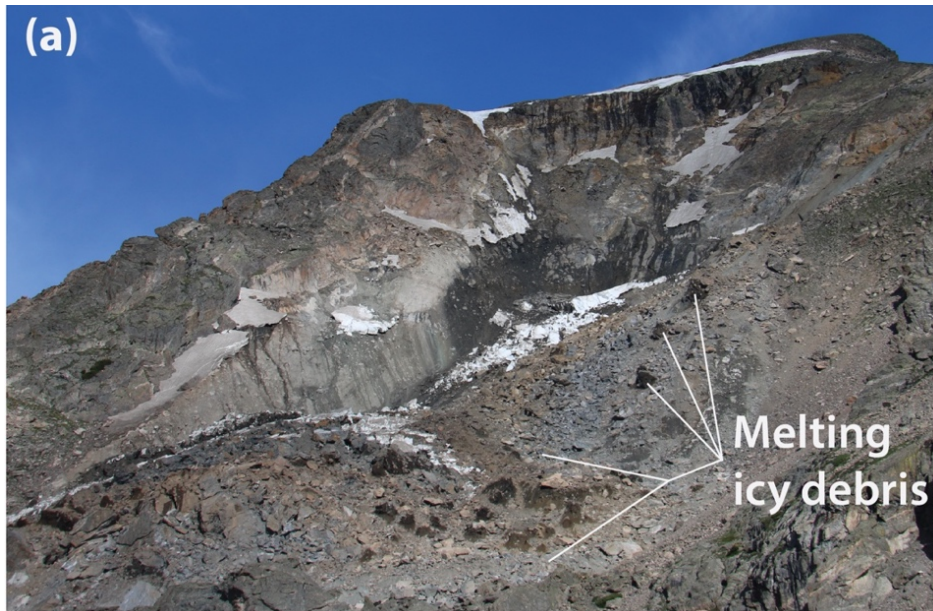
Fig. S9 *Features associated with the 28 June 2022 debris slide (a) Source area and patches of melting icy debris on 5 July 2022, photo taken from location e on Fig. 1, courtesy of Matthew Morriss. (b) View downvalley from the landslide deposits, showing Chaos Canyon rock glacier and Lake Haiyaha. Area labeled "Meadow" is popular with climbers. Distance from foreground to the western edge of Lake Haiyaha is about 1 km. Photo taken on 15 July 2022 from UAV flight over the debris slide from location a on Fig. 1.*

Fig. S10 *Photo taken by the UAV on 15 July 2022 looking down the landslide from near the headscarp, showing the debris flows flowing into a pool impounded behind a dam of debris and snow 'boulders,' with some flows going around the right side onto the lower active debris flow fan.*

Fig. S11 *Photo of the upper part of the landslide taken by hikers about 6 weeks after the landslide (9 August 2022) showing its condition later in the summer. All the remnants of the snowfield have melted and only the southwest corner of the source area is still seeping. Black arrows indicate the fracture at the top of the remaining wedge of debris mentioned in the main text. The 28 June landslide scarp is to the left of this area. Photo courtesy of Pete Miller.*

References

9news.com (2022) Hallett Peak rockslide in Rocky Mountains National Park captured by hiker. https://www.9news.com/video/sports/outdoors/hallett-peak-rockslide-in-rocky-mountains-national-park-captured-by-hiker/73-2c76e565-9ab1-4cf4-a985-39ea7e229fad. Accessed 24 Feb 2023

Agisoft, LLC (2023) Agisoft Metashape 1.8.5. https://www.agisoft.com/

Benz HM, McMahon ND, Aster RC, et al (2015) Hundreds of earthquakes per day: The 2014 Guthrie, Oklahoma, earthquake sequence. Seismol Res Lett 86:1318–1325. https://doi.org/10.1785/0220150019

Brunet M, Moretti L, Le Friant A, et al (2017) Numerical simulation of the 30–45 ka debris avalanche flow of Montagne Pelée volcano, Martinique: From volcano flank collapse to submarine emplacement. Nat Hazards 87:1189–1222. https://doi.org/10.1007/s11069-017-2815-5

Bouchut F, Mangeney-Castelnau A, Perthame B, Vilotte J-P (2003) A new model of Saint Venant and Savage–Hutter type for gravity driven shallow water flows. Comptes Rendus Math 336:531–536. https://doi.org/10.1016/S1631-073X(03)00117-1

Bouchut F, Westdickenberg M (2004) Gravity driven shallow water models for arbitrary topography. Commun Math Sci 2:359–389

Caplan-Auerbach J, Huggel C (2007) Precursory seismicity associated with frequent, large ice avalanches on Iliamna volcano, Alaska, USA. J Glaciol 53:128–140. https://doi.org/10.3189/172756507781833866

Corominas J (1996) The angle of reach as a mobility index for small and large landslides. Can Geotech J 33:260–271. https://doi.org/10.1139/t96-005

Delannay R, Valance A, Mangeney A, et al (2017) Granular and particle-laden flows: From laboratory experiments to field observations. J Phys Appl Phys 50:053001. https://doi.org/10.1088/1361-6463/50/5/053001

Durand V, Mangeney A, Haas F, et al (2018) On the link between external forcings and slope instabilities in the Piton de la Fournaise summit crater, Reunion Island. J Geophys Res Earth Surf 123:2422–2442. https://doi.org/10.1029/2017JF004507

EDF R&D (2023) CloudCompare (v 2.13.0) [GPL software]. http://www.cloudcompare.org/

Edwards AN, Viroulet S, Kokelaar BP, Gray JMNT (2017) Formation of levees, troughs and elevated channels by avalanches on erodible slopes. J Fluid Mech 823:278–315. https://doi.org/10.1017/jfm.2017.309

Favreau P, Mangeney A, Lucas A, et al (2010) Numerical modeling of landquakes. Geophys Res Lett 37:L15305. https://doi.org/10.1029/2010GL043512

Galas S, Dalbey K, Kumar D, et al (2007) Benchmarking TITAN2D mass flow model against a sand flow experiment and the 1903 Frank Slide. In: Proceedings of the 2007 International Forum on

Landslide Disaster Management. Edited by Ho and Li. Hong Kong Geotechnical Engineering Office. pp 899–918

Garres-Díaz J, Fernández-Nieto ED, Mangeney A, Morales de Luna T (2021) A weakly non-hydrostatic shallow model for dry granular flows. J Sci Comput 86:25. https://doi.org/10.1007/s10915-020-01377-9

GDR MiDi (2004) On dense granular flows. Eur Phys J E 14:341–365. https://doi.org/10.1140/epje/i2003-10153-0

Harris DB (2006) Subspace detectors: Theory. Lawrence Livermore Natl Lab Tech Rep UCRL-TR-222758: https://doi.org/10.2172/900081

Hayashi JN, Self S (1992) A comparison of pyroclastic flow and debris avalanche mobility. J Geophys Res Solid Earth 97:9063–9071. https://doi.org/10.1029/92JB00173

Heim A (1932) Bergsturz und menschenleben. Fretz & Wasmuth

Hsü KJ (1975) Catastrophic debris streams (sturzstroms) generated by rockfalls. Geol Soc Am Bull 86:129. https://doi.org/10.1130/0016-7606(1975)86<129:CDSSGB>2.0.CO;2

Hungr O, Corominas J, Eberhardt E (2005) Estimating landslide motion mechanism, travel distance and velocity. In: Landslide Risk Management. CRC Press

Jaboyedoff M, Carrea D, Derron M-H, et al (2020) A review of methods used to estimate initial landslide failure surface depths and volumes. Eng Geol 267:105478. https://doi.org/10.1016/j.enggeo.2020.105478

Lague D, Brodu N, Leroux J (2013) Accurate 3D comparison of complex topography with terrestrial laser scanner: Application to the Rangitikei canyon (N-Z). ISPRS Journal of Photogrammetry and Remote Sensing 82:10–26. https://doi.org/10.1016/j.isprsjprs.2013.04.009

Léopoldès J, Jia X, Tourin A, Mangeney A (2020) Triggering granular avalanches with ultrasound. Phys Rev E 102:042901. https://doi.org/10.1103/PhysRevE.102.042901

Legros F (2002) The mobility of long-runout landslides. Eng Geol 63:301–331. https://doi.org/10.1016/S0013-7952(01)00090-4

Lucas A, Mangeney A, Ampuero JP (2014) Frictional velocity-weakening in landslides on Earth and on other planetary bodies. Nat Commun 5:3417. https://doi.org/10.1038/ncomms4417

Mangeney A, Bouchut F, Thomas N, et al (2007) Numerical modeling of self-channeling granular flows and of their levee-channel deposits. J Geophys Res Earth Surf 112:. https://doi.org/10.1029/2006JF000469

Mangeney-Castelnau A, Bouchut F, Vilotte JP, et al (2005) On the use of Saint Venant equations to simulate the spreading of a granular mass. J Geophys Res Solid Earth 110:. https://doi.org/10.1029/2004JB003161

McDougall S (2017) 2014 Canadian Geotechnical Colloquium: Landslide runout analysis — current practice and challenges. Can Geotech J 54:605–620. https://doi.org/10.1139/cgj-2016-0104

Peruzzetto M, Mangeney A, Bouchut F, et al (2021) Topography curvature effects in thin-layer models for gravity-driven flows without bed erosion. J Geophys Res Earth Surf 126:e2020JF005657. https://doi.org/10.1029/2020JF005657

Peruzzetto M, Mangeney A, Grandjean G, et al (2020) Operational estimation of landslide runout: Comparison of empirical and numerical methods. Geosciences 10:424. https://doi.org/10.3390/geosciences10110424

Poli P (2017) Creep and slip: Seismic precursors to the Nuugaatsiaq landslide (Greenland). Geophys Res Lett 44:8832–8836. https://doi.org/10.1002/2017GL075039

Poulain P, Friant AL, Mangeney A, et al (2023) Performance and limits of a shallow-water model for landslide-generated tsunamis: from laboratory experiments to simulations of flank collapses at Montagne Pelée (Martinique). Geophys J Int 233:796–825. https://doi.org/10.1093/gji/ggac482

QGIS.org, (2022). QGIS Geographic Information System v3.16. QGIS Association. http://www.qgis.org

Rengers FK, Reitman NG, Brady LR, et al (2023) UAV imagery and digital elevation model for the debris slide in Chaos Canyon, 28 June 2022, Rocky Mountain National Park, Colorado. US Geol Surv Data Release. https://doi.org/10.5066/P9ZQQY3G

Scheidegger AE (1973) On the prediction of the reach and velocity of catastrophic landslides. Rock Mech 5:231–236. https://doi.org/10.1007/BF01301796

Terzaghi K, Peck RB, Mesri G (1996) Soil mechanics in engineering practice. John Wiley & Sons

Toney L, Fee D, Allstadt KE, et al (2021) Reconstructing the dynamics of the highly similar May 2016 and June 2019 Iliamna Volcano (Alaska) ice–rock avalanches from seismoacoustic data. Earth Surf Dyn 9:271–293. https://doi.org/10.5194/esurf-9-271-2021

U.S. Geological Survey (2022) USGS 1 Meter 13 x44y447 CO_DRCOG_2020_B20. US Geol Surv Data Release. https://www.sciencebase.gov/catalog/item/620de575d34e6c7e83baa0d8

Virtanen P, Gommers R, Oliphant TE, et al (2020) SciPy 1.0: Fundamental algorithms for scientific computing in Python. Nature Methods 17:261–272. https://doi.org/10.1038/s41592-019-0686-2

Yamada M, Mori J, Matsushi Y (2016) Possible stick-slip behavior before the Rausu landslide inferred from repeating seismic events. Geophys Res Lett 43:9038–9044. https://doi.org/10.1002/2016GL069288